Zero electron kinetic energy and photoelectron spectroscopy of the XeI^- anion

Thomas Lenzer, Michael R. Furlanetto, Knut R. Asmis, and Daniel M. Neumark
Department of Chemistry, University of California, Berkeley, California 94720
and Chemical Sciences Division, Lawrence Berkeley National Laboratory, Berkeley, California 94720

(Received 6 July 1998; accepted 15 September 1998)

The XeI^- anion and the corresponding neutral $X1/2$, $I3/2$, and $II1/2$ electronic states have been studied by means of zero electron kinetic energy (ZEKE) and photoelectron spectroscopy. The ZEKE spectra show rich and well-resolved progressions in the low-frequency vibrations of the anion and the neutral van der Waals complexes. From our spectroscopic data we construct model potentials for the anion and three neutral states, which are compared to previously obtained potential functions for this system. The intensity of the $I3/2 \leftarrow$ anion transitions relative to the $X1/2 \leftarrow$ anion transitions in the XeI^- ZEKE spectrum is considerably lower than expected from a Franck-Condon simulation based on the model potentials. Comparison with the photoelectron spectrum of XeI^- indicates this is due to a small *s*-wave partial cross section for photodetachment to the $I3/2$ state. © *1998 American Institute of Physics.* [S0021-9606(98)00148-2]

I. INTRODUCTION

The characterization of the potential energy function between weakly interacting species has been the subject of extensive experimental and theoretical effort over the past decades. As a result, many key features governing the interaction between closed shell neutral species are now well understood both experimentally and theoretically.[1–3] However, considerably less is known about the interactions between open and closed shell species with their manifold of available potential energy surfaces. A similar statement holds for the intermolecular forces between ions and neutrals, where from the experimental point of view the implementation of sensitive spectroscopic techniques with adequate resolution is far from straightforward. Although high-frequency, intramolecular vibrational modes in ion-neutral clusters have been characterized by a variety of infrared action spectroscopy experiments,[4–11] the low-frequency modes characteristic of ion-neutral binding are more difficult to observe.

For negatively charged species, the development of anion ZEKE (zero electron kinetic energy) spectroscopy[12] (based on the original design for the photoionization of neutrals as introduced by Schlag and co-workers[13–15]) has proven to be a powerful means of characterizing the low-frequency vibrational modes involved in weak ion-neutral interactions. Rare gas halides (RgX^-) are particularly well-suited for such studies, and ZEKE spectra for $KrBr^-$, $XeBr^-$, $KrCl^-$,[16] KrI^-, ArI^-, $ArBr^-$,[17] as well as the larger clusters Ar_nI^- ($n=2-19$) and Ar_nBr^- ($n=2-9$),[18] have already been investigated in this laboratory. The present study on XeI^- is a continuation of this work and part of the ongoing effort in our group to obtain anion ZEKE spectra for the complete RgX^- series.

The charged Rg_nX^- species represent the simplest solvated ionic chromophores and are therefore important prototypical systems for understanding the influence of the surrounding on the photophysical properties and reactivity of ions in solution. ZEKE spectroscopy of the RgX^- diatomics yields accurate pair potentials, which are needed as a reliable basis to quantitatively assess the structure, energetics and dynamics of larger halide clusters,[18,19] as well as the importance of many-body effects in these and related systems.[18] From a more practical standpoint the RgX^- interaction potentials determine the transport properties of halide ions in rare gases, and are, for instance, important for the understanding and modeling of processes in plasmas and discharges.

As far as the XeI^- anion is concerned, the only experimental information available so far comes from photoelectron spectra and photodetachment action spectra of Cheshnovsky and co-workers, who obtained electron binding energies for Xe_nI^- clusters up to $n=12$.[20] However, no experimental data on the interaction potential of XeI^- exist, and the only available information in this respect comes from coupled cluster calculations,[21] the scaled electron gas theory,[22] and various (semi-)empirical models.[23–26]

The interactions in neutral RgX complexes are particularly interesting, because they represent textbook examples of open shell – closed shell interactions. Three molecular electronic states arise from the ^2P halogen atom–rare gas interaction, as shown in Fig. 1.[27,28] The lower $^2P_{3/2}$ state is split by the electrostatic interaction into two components, corresponding to the two possible projections of the total electronic angular momentum Ω along the internuclear axis: $\Omega=1/2$ (the $X1/2$ state or ''X'' state in the notation used here) and $\Omega=3/2$ (the $I3/2$ or ''I'' state). The upper $^2P_{1/2}$ halogen spin-orbit state correlates with the $II1/2$ state ($=$''II'' state) in the complex ($\Omega=1/2$).

Although these interactions are in general fairly weak, especially when compared to chemical forces in reactive processes, their influence on reaction dynamics can be significant, as shown in recent quantum mechanical and quasiclas-

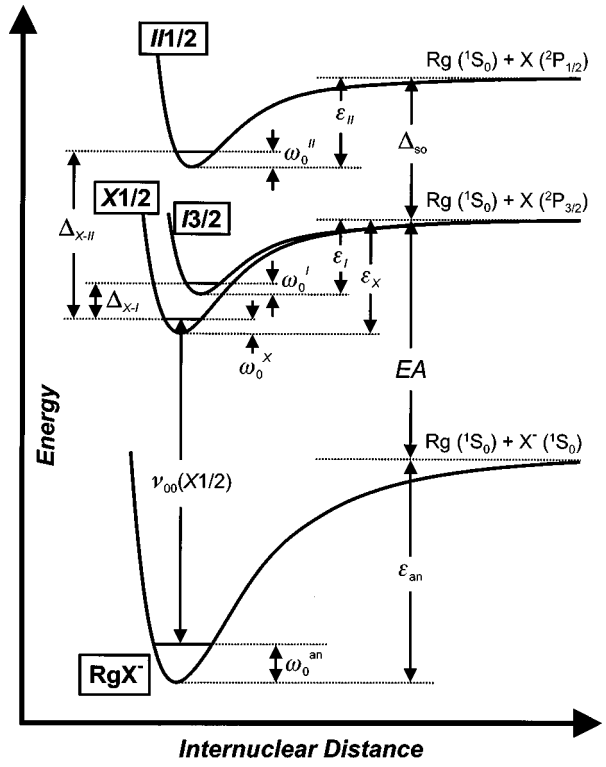

FIG. 1. Schematic diagram of potential energy levels involved in the photodetachment of rare gas halides (RgX^-). The energetic relations among the atomic and molecular anion and neutral electronic states are shown. For a description of the various quantities see Sec. IV B.

sical trajectory calculations of the ''one-atom cage effect'' in $I_2Ar(B)$.[29,30] A detailed characterization of such interactions is therefore highly desirable.

The practical importance of several members of the neutral RgX series originates from their use in excimer lasers (the most prominent examples being XeCl, ArF, and KrF). The lasing process is due to transitions between electronically excited, deeply bound charge transfer states (''Rg^+X^-'') and the repulsive wall of the weakly bound covalent ground states.

In the case of XeI the strongest of these transitions ($X \leftarrow B$) has been studied extensively in emission, and was first observed by Ewing and Brau.[31] In a subsequent study, Tellinghuisen *et al.*[32] recorded the strong diffuse ultraviolet emission bands, and quantitatively analyzed the spectrum for the first time, treating the transition from the B to the X state as bound-free. This yielded the curvature and slope of the X state potential in the Franck-Condon region, the latter being apparently steeper than the estimate given by Ewing and Brau.

In a subsequent study, Casassa *et al.*[33] observed the $II \leftarrow B$ transition in emission for the first time: however, no potential function for the II state could be extracted from this experiment. A detailed analysis of the XeI emission spectrum was carried out by Tamagake *et al.*[34] From the simulation of their spectra they extracted very approximate potentials for the X, I, and II states, which were constructed from a combination of earlier *ab initio* results[35] and an additional dispersion term.

Lee and co-workers[36] determined elastic differential cross sections (DCS) for collisions between $I(^2P_{3/2})$ and $Xe(^1S_0)$ in a crossed molecular beams experiment. The measured DCS contain contributions from the X and I states. Individual potential curves for these states were therefore determined by an appropriate mathematical inversion procedure. For the X and I states they extracted well depths of 241 cm^{-1} and 168 cm^{-1}, respectively. However, no information on the II state could be obtained, because the higher $^2P_{1/2}$ spin-orbit state of iodine is not populated under their experimental conditions.

Jones *et al.*[37] measured photoassociation spectra for Xe–I collision pairs. Unfortunately, their bound-free simulations of the highly structured spectra neglected the shallow X state well found in the scattering study. The most recent investigation of XeI came from Tellinghuisen's laboratory,[38] where the $X \leftarrow B$ emission spectrum was recorded for the single isotopomer $^{136}Xe^{127}I$ with much higher resolution than in their previous work.[32] Their study confirmed that this transition is primarily bound-free. However, extensive weak vibrational structure was also found on top of the broad emission, originating from transitions between higher vibrational levels of the B state and the bound region of the X state. This study yielded a complete potential curve for the X state, unambiguously showing that it possesses a well depth of at least 267 cm^{-1}, already exceeding the well depth extracted from the scattering study. Due to uncertainties in the vibrational level numbering, the well may be even deeper.

The results reported here provide a more complete view of the anion and neutral potentials. Anion ZEKE spectroscopy is a very powerful tool in this respect, because photodetachment from the XeI^- anion allows us to extract detailed information about the anion, as well as the neutral X, I, and II states. The capability of probing the anion and II states is particularly important due to the almost total lack of spectroscopic information.

We have organized this paper as follows: In Sec. II we briefly describe the experimental setup used for studying the XeI^- anion, and in Sec. III our ZEKE spectra are presented and complete assignments are given. Section IV deals with the construction of model potentials for fitting the vibrational and rotational contours of the ZEKE spectra. Finally, in Sec. V we compare our potentials to the available data from theoretical calculations and (semi-)empirical approaches. Special attention is paid to the observed relative intensities of the transitions to the different neutral electronic states in the ZEKE spectra. We also present XeI^- anion photoelectron spectra recorded for comparison with the ZEKE results for the X and I states.

II. EXPERIMENT

The anion zero electron kinetic energy (ZEKE) spectrometer has been described in detail previously,[12,39–41] and only the specific details relevant to this study will be considered here. Briefly, XeI^- anions are generated by passing a mixture of 10%–20% Xe in Ar over CH_3I (0 °C), which is then expanded into vacuum through a 0.5 mm aperture in a pulsed valve (General Valve Series 9), typically applying a backing pressure of 10–30 psi.

The expansion is crossed just in front of the valve by an 1 keV electron beam. Anions are formed through dissociative attachment (and other secondary processes), and undergo clustering in the continuum flow region of the free-jet expansion. The negative cluster ions formed during these processes are effectively cooled as the expansion progresses, and then pass through *two* skimmers into a differentially pumped region. In our setup, the additional second skimmer in the source chamber, placed close (1–2 mm) to the beam valve and about 10 mm away from the first skimmer, is found to substantially enhance the amount of all clusters, especially the larger ones, suggesting an additional cooling effect.

The clusters are then accelerated to 1 keV into a 1 m collinear time-of-flight mass spectrometer, where they separate according to their mass. After entering the detector region the XeI^- anions are photodetached by an excimer-pumped dye laser (Lambda Physik FL3002). In contrast to previous work carried out on this instrument,[12] a weak dc field of -15 mV/cm is applied across the electron detachment region at all times; the negative sign indicates the field is anti-parallel to the ion beam propagation direction, so that this field slightly decelerates electrons in the laboratory frame.

After a delay of 200–500 ns, the electrons are extracted coaxially to the ion beam by applying a pulsed extraction field of 4 V/cm across the extraction region. Higher energy electrons with velocity components perpendicular to the ion beam axis are discriminated against geometrically by the extraction plates acting as apertures. The electrons with (nearly) zero kinetic energy and the higher energy electrons ejected forward and backward on axis travel different distances in the extraction field and gain different amounts of energy. They therefore separate in the following drift region, and those electrons having nearly zero electron kinetic energy relative to the anion packet can be selectively detected in a 35–100 ns wide temporal gate using a microchannel plate detector positioned approximately 1 m away from the extraction region.

The addition of a weak dc field enhances the amount of ZEKE electrons by roughly a factor of three, with no degradation of the spectral resolution of 1–2 cm^{-1} for atomic anions. The peaks observed in this study are broader than this because they consist of unresolved rotational envelopes. Also, slightly shorter extraction delays than required for maximum resolution are used in this study, leading to a slight decrease in resolution but more rapid data acquisition. The experiment is operated at a repetition rate of 30 Hz. For studying the *X* and *I* states QUI dye (Exciton) is used with a typical energy of 30 mJ/pulse. For the *II* state the dye laser fundamental (Rhodamine 610, Exciton) is doubled in a KDP crystal, yielding laser pulse energies of about 2–3 mJ. The ZEKE spectra are normalized to the ion signal and laser power, and averaged over 2000–4000 laser shots per point. Absolute vacuum wavelengths are obtained by calibration of the dye laser either with a New Focus 7711 Fizeau wavelength meter (*X* and *I* states) or a Fe/Ne hollow cathode lamp (*II* state).

The time-of-flight anion photoelectron spectrometer has already been described at length elsewhere.[42,43] XeI^- anions are produced using the same mixture as noted above. However, in this case only a single skimmer (1 mm diameter) in conjunction with higher backing pressures (40–80 psi) is used. The ions are extracted from the beam and then enter a time-of-flight mass spectrometer with a linear reflectron stage.

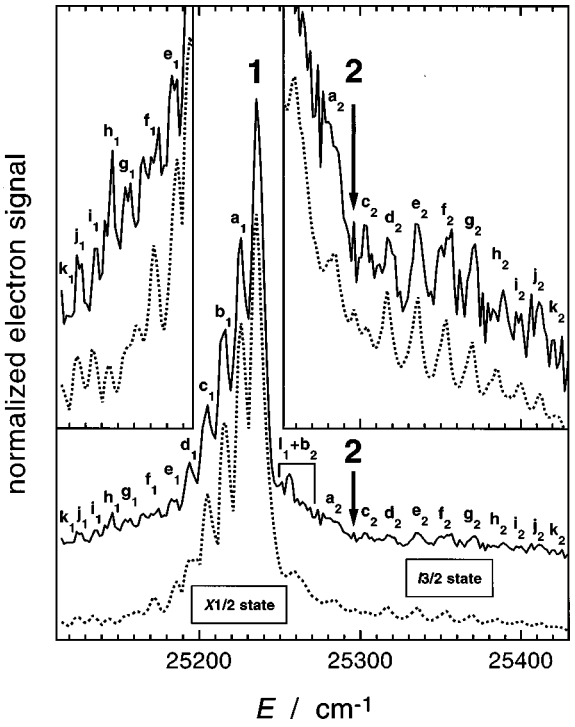

FIG. 2. Experimental and simulated XeI^- ZEKE spectra for the $X1/2$ and $I3/2$ states ($^2P_{3/2}$ asymptote). Solid lines: experimental data; dotted lines: best fit spectral simulation based on MMSV model potentials, as described in text. Peaks **1** and a_1-l_1 belong to the *X* state and peaks **2** and a_2-k_2 to the *I* state; see Tables I and II for complete assignments of all features. The two insets on the left and on the right show magnifications of the experimental and simulated spectra in the corresponding energy regions.

The ions separate in time and space according to their mass-to-charge ratios, and the XeI^- ions are then selectively detached by the third harmonic of a pulsed Nd:YAG laser (355 nm corresponding to 3.493 eV; Quanta-Ray DCR-3), running at 20 Hz. The energy of the photoelectrons is measured by time-of-flight in a field-free flight tube 100 cm in length. The instrumental resolution under these conditions (electron kinetic energy around 0.4 eV) is about 8 meV. The polarization dependence of the features in the XeI^- photoelectron spectra is investigated by varying the angle θ between the laser polarization and the direction of electron collection, using a half-wave plate. In this way, photoelectron spectra at $\theta = 0°$ and 90° (''horizontal'' and ''vertical'' polarization, respectively) are obtained.

III. ZEKE SPECTRA AND ASSIGNMENTS

As is already clear from the remarks in Sec. I and Fig. 1, we expect to observe two band systems, which are separated by approximately the spin-orbit constant of atomic iodine (0.942 65 eV=7603.0 cm^{-1}).[44] The lower energy band system is shown in Fig. 2, and results from transitions to the

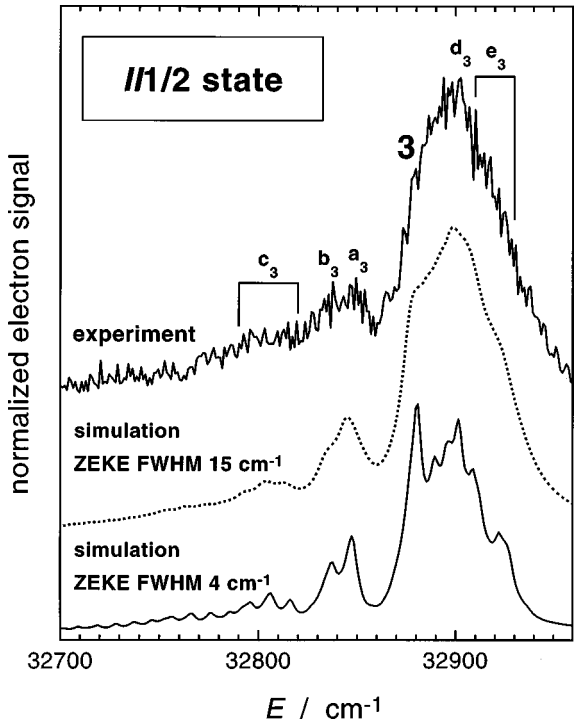

FIG. 3. Experimental and simulated XeI^- ZEKE spectra for the $II1/2$ state ($^2P_{1/2}$ asymptote). Upper solid line: experimental data (lower resolution than in the spectrum of Fig. 2); dotted line: best fit spectral simulation with a ZEKE peak FWHM of 15 cm^{-1}, based on MMSV model potentials, as described in text; lower solid line: same spectral simulation but with a smaller ZEKE peak FWHM of 4 cm^{-1}, corresponding to the same resolution assumed as in the simulation of Fig. 2. For complete assignments of features **3** and a_3-e_3 see Table III.

$X1/2$ and $I3/2$ states. The higher energy system in Fig. 3 is due to the $II1/2$ state.

The experimental spectrum in Fig. 2 (solid line) shows a very rich structure and more peaks than were observed in the ZEKE studies of ArI^- and KrI^-.[17] We achieve complete assignment of virtually all the features by our spectral simulation (dotted line in Fig. 2 and Tables I and II). While specific details of this simulation will be amply discussed in Sec. IV, we will refer to some of the results of this analysis in the following assignment of the spectral features.

The XeI^- anion vibrational frequency is expected to be considerably larger than for each of the three neutral XeI states, and this allows us to distinguish among three types of neutral←anion transitions ($\Delta v = v'$-v'') which contribute to the spectra: vibrational v' progressions in the neutral originating from a single anion vibrational level v'', sequence band transitions with *constant* Δv from a series of anion vibrational levels ($\Delta v = 0$ and -2 are the most prominent observed in this study), and single hot band transitions ($\Delta v \neq 0$) from vibrationally excited anion levels. The first type of transition occurs at higher energy than the origin (0-0 transition) of a particular electronic band, while the other two occur at lower energy.

The region below 25 250 cm^{-1} is dominated by one peak, labeled **1**, with a number of smaller peaks, denoted as a_1 to k_1, of decreasing intensity appearing toward lower energy. We assign peak **1** to the origin (0-0) transition from the anion to the X state. The prominent peaks a_1 to e_1 are nearly equally spaced, by roughly 10 cm^{-1}, and are assigned to $\Delta v = 0$ sequence band transitions from vibrationally excited anion states, i.e., the 1-1 to 5-5 transitions.

At even lower energy, peaks g_1 to k_1, which are also equally spaced by about 10 cm^{-1}, are assigned to the $\Delta v = -2$ sequence band (2-4 to 6-8, the last one only partially recorded). For the sake of clarity this spectral region has been magnified in the left inset of Fig. 2. Note that the region of peaks $f_1 - g_1$ looks somehow more irregular than the rest, both in the experimental and simulated spectrum, which is due to the overlap of several transitions (see Table I for complete assignments).

The large intensity of the X←anion 0-0 transition and the total absence of visible progressions in the neutral originating from the anion vibrational ground state already suggest very similar equilibrium bond lengths of the anion and the X state, as was seen in all our previous studies on RgX^- species.[16,17] However, the XeI^- ZEKE spectrum shows

TABLE I. Peak assignments for the $X1/2$←anion transitions in the XeI^- ZEKE spectrum (left part of Fig. 2). All energies are in cm^{-1}. The assignment listed first contributes the most to the peak intensity. Assignments in parentheses are additional transitions needed to account for at least two third of the total peak intensity, listed in order of decreasing magnitude of their contribution.

Peak	Position	Relative energy	v' ($X1/2$)←v'' (anion) assignment	
1	25 235.9	0.0	0←0	
a_1	25 225.7	−10.2	1←1	
b_1	25 215.3	−20.6	2←2	
c_1	25 204.8	−31.1	3←3	
d_1	25 194.2	−41.7	4←4	
e_1	25 184.1	−51.8	5←5	(7←6)
f_1 (broad)	25 169.8	−66.1	8←7	(10←8, 1←3, 6←6)
g_1	25 155.9	−80.0	2←4	(9←8, 11←9)
h_1	25 145.1	−90.8	3←5	
i_1	25 136.2	−99.7	4←6	
j_1	25 126.1	−109.8	5←7	
k_1	25 115.3	−120.6	6←8	
l_1 (broad)	25 256.0	+20.1	4←2	(6←3)

TABLE II. Peak assignments for the $I3/2$←anion transitions in the XeI^- ZEKE spectrum (right part of Fig. 2). All energies are in cm^{-1}. The assignment listed first contributes the most to the peak intensity. Assignments in parentheses are additional transitions needed to account for at least two third of the total peak intensity.

Peak	Position	Relative energy	v' ($I3/2$)←v'' (anion) assignment	
2	25 295.9	0.0	0←0	
a_2	25 282.8	−13.1	1←1	
b_2	25 263.4	−32.5	0←1	(3←3)
c_2	25 303.1	+7.2	2←1	(4←2)
d_2	25 316.8	+20.9	1←0	
e_2	25 335.3	+39.4	2←0	
f_2	25 352.9	+57.0	3←0	
g_2	25 369.6	+73.7	4←0	
h_2	25 385.7	+89.8	5←0	
i_2	25 399.8	+103.9	6←0	
j_2	25 412.0	+116.1	7←0	
k_2	25 423.4	+127.5	8←0	

many more lines than our previous spectra of other RgX^- anions, indicating a higher vibrational temperature. We estimate $T_{vib} \approx 160$ K and $T_{rot} \approx 100$ K from our fit, compared, e.g., to $T_{vib} \approx 60-80$ K and $T_{rot} \approx 40$ K in our $ArI^-/KrI^-/ArBr^-$ anion ZEKE study.[17] While the reason for this higher temperature is not entirely clear, the observation of more spectral features does allow a more detailed characterization of the anion and neutral states.

The spectral features in Fig. 2 above 25 250 cm^{-1} are due to $I3/2 \leftarrow$ anion transitions. Only *very* weak lines are observed over the whole energy range. A second inset has been included in the upper right half of the figure, showing a magnification of this part of the experimental spectrum and the corresponding spectral simulation. The following assignments are made primarily because they give the best fit involving the optimized *I* state model potential, and at the same time are the ones that are most consistent with the parameters extracted for the anion and *II* state potentials (Sec. IV C).

Peaks **2**, $d_2, \ldots, g_2$ are assigned to a vibrational progression in the *I* state, with peak **2** assigned as the 0-0 transition and the latter four peaks as $(v'\text{-}0)$ transitions with $v' = 1-4$. With the help of the simulation one can extend this progression up to $v' = 8$ (peaks h_2-k_2). The extent of this progression indicates that the bond length of the *I* state is significantly different from the anion, in apparent contrast to the *X* state. Moreover, the overall intensity of the *I* band is much lower than expected from the simulated Franck-Condon factors alone, as will be further addressed in Sec. V B. Complete assignments of all the $I3/2 \leftarrow$ anion transitions can be found in Table II. The assignment of the barely visible peak **2** to the 0-0 transition is supported by the observation of peak c_2 and its assignment to the 2-1 transition.

The ZEKE spectrum for photodetachment to the $II1/2$ state is shown in Fig. 3 (upper solid line). The resolution in this case is worse than for the *X* and *I* states, because the delay between photodetachment and electron extraction was significantly reduced to about 200 ns in order to achieve acceptable signal rates. This results in a ZEKE linewidth of roughly 15 cm^{-1}, due to poorer discrimination against higher energy electrons. The small signal results from the combination of much lower detachment laser power (frequency doubling was required), and the inherently low intensity of the *II* state, which seems to be comparable to the *I* state.

Our anion ZEKE spectrum therefore more or less shows the band envelope, but no sharp individual peaks are seen, and thus any assignment must rely on the fit to the potential described in Sec. IV. In Fig. 3 two simulations have been included. The middle (dotted) simulation represents the fit using the actual resolution of the *II* state experiments, while the lower one shows a simulated spectrum as it would appear if the resolution were the same as in the *X* and *I* spectra (Fig. 2). The simulation locates the *II* state 0-0 transition (**3**) on the left edge of the broad main peak centered around 32 900 cm^{-1}. At lower energy a second broader feature near 32 850 cm^{-1} is visible (peaks a_3 and b_3) due to the 0-1 and 1-2 hot band transitions. The maximum and right shoulder of the main peak (d_3 and e_3) are due to several neutral progressions $(v'\text{-}0$ and $v'\text{-}1)$. See Table III for a compilation of all individual $II \leftarrow$ anion transitions.

TABLE III. Peak assignments for the $II1/2 \leftarrow$ anion transitions in the XeI^- ZEKE spectrum (Fig. 3). All energies are in cm^{-1}. Only approximate values can be given with the aid of the spectral simulation due to the reduced experimental resolution in this case (see text). For particularly broad features the transitions contributing the most to the total peak intensity are given.

Peak	Position	Relative energy	v' $(II1/2) \leftarrow v''$ (anion) assignment
3	32 880	0	$0 \leftarrow 0$
a_3	32 850	−30	$0 \leftarrow 1$
b_3	32 840	−40	$1 \leftarrow 2$
c_3	32 820–32 790	−60 to −90	$0 \leftarrow 2$, $1 \leftarrow 3$, $2 \leftarrow 4$
d_3	32 902	+22	$1 \leftarrow 0$
e_3	32 910–32 930	+30 to +50	$3 \leftarrow 1$, $5 \leftarrow 2$, $2 \leftarrow 0$, $4 \leftarrow 1$

IV. ANALYSIS

Peak **1** in Fig. 2 yields an accurate electron affinity of $25\,235.9 \pm 2.0$ cm^{-1} for XeI^-, compared to $25\,250 \pm 160$ cm^{-1} obtained from the photoelectron spectrum of Cheshnovsky and co-workers.[20] Note that this value is larger than the corresponding electron affinity for atomic iodine of 24 672.796 cm^{-1}.[45] This shows that the XeI^- dissociation energy is greater than that of XeI. Also, from the vibrational assignments in Tables I–III we can deduce frequencies for the anion and the three neutral states. To gain further insight into the binding properties of the different XeI species (especially the anion and *II* state potentials, for which no high quality data exist) we construct sufficiently flexible *model potentials* for the anion and neutral complexes. The eigenfunctions of these potentials and Franck-Condon factors are then calculated, resulting in a vibrational stick spectrum, which is convoluted with the rotational and ZEKE line shapes to produce a simulated ZEKE spectrum. By iteratively adjusting the potential parameters the best possible fit to the experimental ZEKE spectrum is sought. Finally, we consider the uncertainties in the potential parameters obtained from the best fit.

A. Potential functions

As in previous work,[16,17,36] we use the flexible, piecewise Morse–Morse-switching function-van der Waals (MMSV) potential to fit our spectra. For neutral XeI, the reduced form of this potential [with $f(x) = V(R)/\epsilon$ and $x = R/R_m$] is:

$$\begin{aligned} f(x) &= e^{2\beta_1(1-x)} - 2e^{\beta_1(1-x)}, \quad 0 < x \leqslant 1, \\ &= e^{2\beta_2(1-x)} - 2e^{\beta_2(1-x)} \equiv M_2(x), \quad 1 < x \leqslant x_1, \\ &= SW(x)M_2(x) + [1 - SW(x)]W(x), \quad x_1 < x < x_2, \\ &= -C_{6r}x^{-6} - C_{8r}x^{-8} \equiv W(x), \quad x_2 \leqslant x < \infty, \end{aligned} \tag{1}$$

where the switching function is given by

$$SW(x) = \frac{1}{2}\left[\cos\frac{\pi(x-x_1)}{(x_2-x_1)} + 1\right], \tag{2}$$

TABLE IV. Dipole and quadrupole polarizabilities and effective numbers of electrons used to calculate dispersion and induction coefficients.

Atom	Corresponding spinless state of XeI neutral	α_d [a_0^3]	α_q [a_0^5]	N
I	Σ	30.05[a]	266.7[b]	6.5[c]
	Π	34.57[a]	314.5[b]	6.5[c]
Xe	---	27.16[d]	202.8[e]	7.253[f]

[a]Derived from the spherically averaged α_d(I) value (Ref. 47) assuming the same anisotropy as for α_d(Cl) (Ref. 50).
[b]Derived from the spherically averaged α_q(I) value assuming the same anisotropy as for α_q(Cl) (Ref. 51). Spherically averaged α_q(I) value itself calculated via the ''hydrogenic relationship'' (Ref. 52) using α_d(I) from Ref. 47.
[c]Reference 47.
[d]Reference 48.
[e]Reference 49.
[f]Calculated from the C_6 value of Ref. 48.

and the reduced dispersion coefficients C_{nr} take the form:

$$C_{6r}=\frac{C_6}{\epsilon R_m^6}, \quad C_{8r}=\frac{C_8}{\epsilon R_m^8}. \tag{3}$$

Here, ϵ is the potential well depth and R_m represents the equilibrium bond length (=position of the well minimum). C_6 is the induced dipole–induced dipole dispersion coefficient, and C_8 represents the corresponding coefficient for the induced dipole–induced quadrupole interaction. Higher dispersion terms are neglected, as is the small induction term, varying as R^{-8}, due to the permanent quadrupole moment of the iodine atom. The XeI^- anion potential is of the same form, except that the dispersion terms are replaced by:

$$f(x)=-B_{4r}x^{-4}-B_{6r}x^{-6}\equiv W(x), \quad x_2\leqslant x<\infty, \tag{4}$$

with

$$B_{4r}=\frac{B_4}{\epsilon R_m^4}, \quad B_{6r}=\frac{B_6}{\epsilon R_m^6}. \tag{5}$$

and

$$B_4=\tfrac{1}{2}q^2\alpha_d(\mathrm{Xe}), \quad B_6=\tfrac{1}{2}q^2\alpha_q(\mathrm{Xe})+C_6. \tag{6}$$

Here, q represents the iodide charge and B_4 is the coefficient of the leading term in the long range XeI^- potential, reflecting the dipole induced in the Xe atom by I^-. The B_6 term arises from quadrupole induction and dipole dispersion terms. α_d(Xe) and α_q(Xe) are the dipole and quadrupole polarizabilities of the Xe atom, respectively; these are given in Table IV.

The dispersion coefficients C_6 and C_8 for the *neutral* XeI $X1/2$, $I3/2$, and $II1/2$ states are estimated using the formulas of Koutselos and Hason[46] Their formulas involve the dipole and quadrupole polarizabilities of each interacting atom, and an effective number of electrons, N, characteristic of each atom. These quantities were taken from experimental sources,[47,48] semi-empirical approaches,[47,48] or *ab initio* calculations.[49] The anisotropy of the dipole and quadrupole polarizabilities for the I atom is determined in the same manner used by us previously for the Br atom.[16] The relevant parameters are listed in Table IV.[50–52]

The C_6 parameter for the XeI^- *anion* is taken from the *ab initio* calculations of Hättig and Heß[53] who determined dispersion coefficients for the whole series of rare gas halides. Note that all of their *ab initio* C_6 parameters are in excellent agreement with the values published by Koutselos, Mason, and Viehland,[24] which were deduced via an universal scaling scheme for closed shell interactions involving rare gas–rare gas, alkali ion–noble gas, and halogen ion–noble gas interactions. All C_6 and C_8 dispersion coefficients are given together with the other potential parameters in Table V. Because the ZEKE spectra are not sensitive to the very

TABLE V. MMSV potential parameters and deduced spectroscopic constants for XeI and XeI^-. Term values T_0 are referenced to the anion vibrational ground state. ω_0=zero point energy, ν_{01}=fundamental vibrational frequency. Assumed anion temperature in the spectral simulations for $X1/2$,$I3/2$($II1/2$): T_{vib}=160 (160) K and T_{rot}=100 (130) K. Error bars (±) estimated from multiparameter sensitivity analysis as described in text. Parameters given with more digits than are significant to prevent round-off errors. Scattering data also given for comparison.

	$X1/2$	$X1/2$[a]	$I3/2$	$I3/2$[a]	$II1/2$	Anion
T_0 [cm^{-1}]	25 235.9 (2.0)	---	25 295.9 (3.0)	---	32 880 (5)	0
ω_0 [cm^{-1}]	11.98	9.72	10.74	10.21	10.75	16.50
ν_{01} [cm^{-1}]	23.06	19.3	20.18	19.5	21.16	32.45
ϵ [meV][b]	33.07	29.9	25.06	20.8	27.48	103.2
R_m [Å][c]	4.049	4.30	4.34	4.60	4.24	4.09
β_1	$16.8896-8.455\,66\cdot R+1.420\,29\cdot R^2$(0.15)[d]	4.40	7.20 (0.15)	7.10	5.20 (0.15)	3.79 (0.15)
β_2	6.29 (0.15)	6.50	5.95 (0.40)	7.30	7.10 (0.40)	6.03 (0.15)
x_1	1.091 (0.02)	1.1066	1.100 (0.20)	1.0950	1.095 (0.20)	1.010 (0.02)
x_2	1.753 (0.04)	1.800	1.588 (0.20)	1.635	1.635 (0.20)	1.430 (0.04)
C_6 [eV Å^6]	185.5 (28)	214.9	198.4 (30)	214.9	192.0 (29)	---
C_8 [eV Å^8]	1982 (600)	1499	2148 (600)	1499	2065 (600)	---
B_4 [eV Å^4]	---	---	---	---	---	28.98 (4.3)
B_6 [eV Å^6]	---	---	---	---	---	365.4 (110)

[a]Scattering data from Ref. 36.
[b]Possible systematic ϵ shift for all ZEKE potentials of +3 meV per unit if the $X1/2$ state level numbering is off (see Sec. IV A).
[c]Possible systematic R_m shift of about ±0.3 Å for all ZEKE potentials, because experiment is only sensitive to relative differences in R_m.
[d]R dependent β_1 imperative to obtain the best MMSV fit to the Morse–RKR repulsive wall of the potential from Ref. 38.

long range part of the potential, B_4, B_6, C_6, and C_8 were kept fixed at the calculated values during the fitting procedure.

Since we cannot resolve any rotational structure due to our experimental ZEKE resolution of $\geqslant 1$ cm^{-1}, we are not able to independently extract information on the equilibrium bond length of any of the potentials determined in this study. A similar problem holds for the well depth ϵ, because we are only sensitive to the differences between two electronic states. We must therefore refer to other experiments to determine the absolute position and well depth of one of our potential curves. The bond lengths and well depths of the remaining potentials can then be determined with high precision.

Lee and co-workers[36] extracted complete interaction potentials for the $X1/2$ and $I3/2$ states of neutral XeI through elastic differential cross section measurements at two collision energies. These represent the only measurements so far that contain information on the absolute Xe–I bond length. Since scattering on the X and I state potentials contributes to the differential cross section, the two potentials have to be extracted from a (not necessarily unique) inversion procedure. Their quoted error is about $\pm 10\%$ for both ϵ and R_m.

More recently, the $X \leftarrow B$ transition of the $^{136}Xe^{127}I$ isotopomer was studied in emission by Radzykewycz and Tellinghuisen (in the following abbreviated as ''R&T''),[38] with superior resolution than their earlier studies.[32] They observed transitions involving seventeen X state vibrational levels, tentatively assigned as $v'=0-16$, with some uncertainty in the absolute numbering. With their ''minimal'' numbering they obtained a well depth of 267 cm^{-1}, which is already outside the quoted 10% error margin of the scattering result (241 cm^{-1}). The value from the emission studies can *only increase* (e.g., to 292 cm^{-1} or 21% difference, if the numbering is off by one unit). Based on their assumed functional form for the B state, they obtain a value of $R_m=4.049$ Å for the X state, which is 0.25 Å less than the scattering potential but still within the 10% error margin.

We use the R&T X state potential as a starting point for the analysis of our ZEKE spectra The turning points from their study are fit using the MMSV potential form of Eq. (1), with only one slight modification: the low energy part of the repulsive wall from the Morse–RKR potential is not particularly well described by a simple Morse branch with a single constant parameter β_1. We have therefore chosen a polynomial of the form $\beta_1=B_0+B_1\cdot R+B_2\cdot R^2$ for the Morse parameter, where B_0, B_1, and B_2 are optimized to give the best fit to the left branch of their curve up to $v'=11$.

The resulting fit employing a Levenberg–Marquardt least-squares fitting algorithm[54] is excellent. For the levels $v=0-11$ the R values of the classical turning points of the R&T Morse–RKR potential are reproduced within 0.03% and the average deviation of our eigenvalues from theirs is only 0.09%. This is more than sufficient for our purposes here. All X state MMSV potential parameters can be found in Table V.

B. Fitting procedure

The vibrational eigenvalues and wave functions for the anion and neutral potentials involving a distinct set of parameters are calculated using a discrete variable representation (DVR) procedure[55] based on a basis set of Morse potential eigenfunctions.[56] Then, Franck-Condon factors are calculated, assuming a Boltzmann distribution for the anion vibrational population, and these are used to produce a simulated vibrational stick spectrum. Finally, a rotational simulation is performed to fit the observed asymmetric peak shapes.[17] In this procedure, a set of rotational lines are calculated for each vibrational band, and these are convoluted with the ZEKE instrumental line shape.[16] For further details of the rotational fitting analysis the reader is referred to our previous work.[17]

Because of the accuracy of the R&T X state potential, its parameters are kept constant at the values obtained from our best fit as explained before. To determine ϵ for the anion and the remaining electronic states we use the relationships implied by Fig. 1, namely:

$$\epsilon_{\mathrm{an}}=\nu_{00}(X1/2)+\omega_0^{\mathrm{an}}+\epsilon_X-\omega_0^X-EA, \tag{7}$$

$$\epsilon_I=\epsilon_X-\Delta_{X\text{-}I}-\omega_0^X+\omega_0^I, \tag{8}$$

$$\epsilon_{II}=\epsilon_X+\Delta_{\mathrm{so}}-\Delta_{X\text{-}II}-\omega_0^X+\omega_0^{II}, \tag{9}$$

where $v_{00}(X1/2)$ is the origin of the $X1/2$ state, ω_0^{an}, ω_0^x, etc. represent zero point energies, EA is the electron affinity of the iodine atom, Δ_{so} is the spin-orbit constant in atomic iodine, $\Delta_{X\text{-}I}$ is the $X1/2-I3/2$ state splitting (between the $v=0$ levels), and $\Delta_{X\text{-}II}$ is the $X1/2-II1/2$ state splitting.

Once all well depths are fixed, the potential parameters R_m, β_1, β_2, x_1, and x_2 of the anion, I and II state potentials, the ZEKE linewidth, and the vibrational and rotational temperature are iteratively adjusted by trial-and-error to produce the best agreement between the experimental and simulated ZEKE spectra. The anion potential is constructed first, to fit the $X1/2\leftarrow$anion band. Once this is fixed, the potentials for the I and II states are determined by their respective bands. Thus, even though the $II1/2\leftarrow$anion band is relatively unstructured, we obtain a reasonably precise potential for the II state because the anion potential has been independently determined.

One additional boundary condition is introduced during this procedure. As pointed out by Haberland[28] and Aquilanti,[57,58] the three neutral potentials are not independent from each other, and if one assumes that the iodine spin-orbit splitting Δ_{so} does not vary with the internuclear separation R (or, alternatively, if this dependence was known, which is usually not the case) and given that two of the three neutral potential functions are known, the third potential function can be calculated analytically. The present fits were therefore subjected to the additional restriction that the three potentials must yield an (almost) constant $\Delta_{\mathrm{so}}(R)$ when applying the formulas of Haberland and Aquilanti. This restriction increased the difficulty of finding an optimized fit even further. The iodine spin-orbit splitting $\Delta_{\mathrm{so}}(R)$ for our best set of potential parameters obtained in this way varies by less than 0.2% for $R>4.0$ Å. However, at shorter range it is necessary to allow a somewhat larger variation

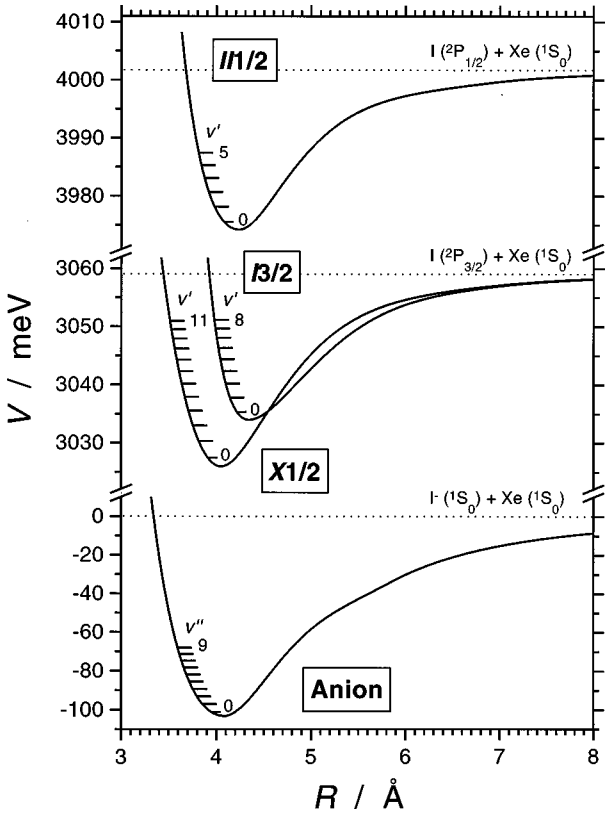

FIG. 4. MMSV model potentials for the XeI^- anion and the XeI neutral $X1/2$, $I3/2$, and $II1/2$ states. Anion asymptote for $R\rightarrow\infty$ set to $E=0$, so the X and I states asymptotically converge towards the iodine electron affinity (3059.038 meV, Ref. 45) and the II state asymptote approaches the sum of the iodine electron affinity and the iodine spin-orbit splitting ($\Delta_{so}=942.65$ meV Ref. 44). Note also the two breaks on the energy axis. Vibrational states involved in transitions (Tables I–III) contributing to visible features in the spectra of Figs. 2 and 3 are marked by short dashes originating at the repulsive wall of each state. Note also that the energy scale spanned by the anion potential curve is a factor of three larger than that of the three neutral states.

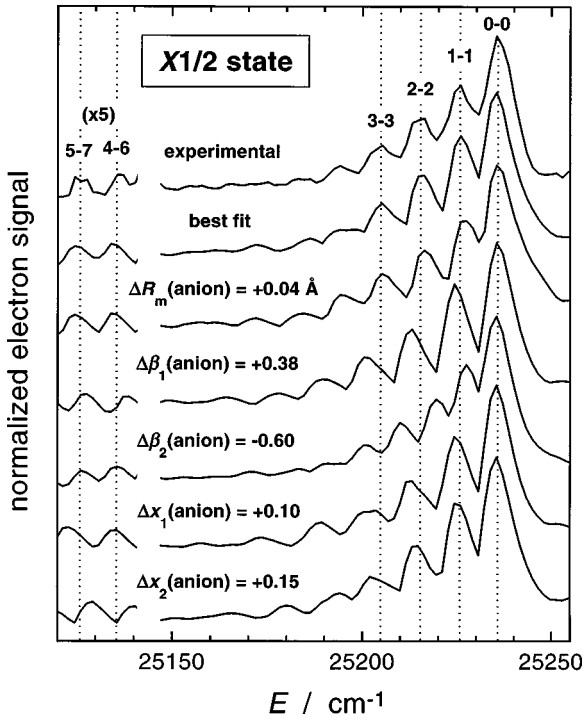

FIG. 5. Sensitivity of the $X1/2\leftarrow$anion ZEKE spectrum simulation to changes in *single* potential parameters of the XeI^- anion. Changes relative to the anion best fit parameters in Table V are given. The remaining parameters of the anion potential and *all* the parameters of the $X1/2$ state potential were kept constant at the values obtained from the best fit (Table V). Characteristic spectral features are marked by dotted lines and their assignments are given (see also Table I). The part of each curve left of the gap is scaled up by a factor of five. Details see text.

which was still less than 3% for $R>3.7$ Å. The deviation at short range corresponds to a slightly smaller Δ_{so} than for atomic iodine.[44] Such a reduction is not unexpected and was also observed for iodine in Xe matrices.[59] Finally we note that if one uses two of the neutral potentials to determine the third, i.e., allowing *no* variation in $\Delta_{so}(R)$, then the repulsive wall of the generated potential deviates significantly from the ''best fit'' potential. This also yields a worse fit of the corresponding ZEKE spectrum.

C. Best fit and sensitivity of its parameters

The best fit potentials are shown in Fig. 4. Note that for a better representation of the well region of the neutral potential curves (preferentially sampled in our ZEKE experiment), the energy scale in the plot for the X, I, and II states (40 meV) is different from that of the anion potential (120 meV). The anion potential is about a factor of three deeper, as the numbers on the energy axis indicate. Also, for all potential curves the vibrational levels contributing to visible transitions in the spectra of Figs. 2 and 3 have been indicated by short dashes on the side of the repulsive walls (see also Tables I–III) and partially numbered.

The best fit parameters of the potentials can be found in Table V, and the corresponding spectral simulations have been included in Figs. 2 and 3. While the assignment of features resulting from this fit has already been discussed in Sec. III, we want to assess in more detail how well the parameters in our potentials are defined.

The possible choice of parameters is highly restricted due to the rich line structure (especially of the X and I states ZEKE spectrum), the interdependence of all potential curves (linked by the common anion electronic state, from which the photodetachment occurs), the imposed energetic restrictions [Eqs. (7)–(9)], and the assumption of an (approximately) R independent iodine spin-orbit splitting. However, one might still argue that the considerable number of adjustable parameters introduces non-negligible uncertainties.

In Fig. 5 we show how the spectral simulation for the $X1/2$ state depends on changes of individual *anion* potential parameters relative to the optimized set. The six vertical dotted lines mark the position of the 0-0 to 3-3 peaks of the $\Delta v=0$ sequence band as well as the 4-6 and 5-7 peaks of the $\Delta v=-2$ sequence band in the experimental and best fit spectrum, and aid in showing shifts in the simulations resulting from varying single parameters. Note that the part of each curve left of the break is scaled up by a factor of five for sake of clarity.

For the following discussion of Fig. 5 we proceed from top to bottom. Increasing R_m of the anion to 4.13 Å (absolute change $+0.04$ Å, corresponding to a relative change of only

1%) reduces the peak spacing of the $\Delta v=0$ sequence band visibly. If one increases the Morse parameter β_1 of the anion repulsive wall to 4.17 (+0.38, 10%), the spacing of the same sequence band increases dramatically. This is understandable, because increasing β_1 increases the steepness of the anion repulsive wall [Eq. (1)] and therefore the anion level spacing (vibrational frequency). The next simulation results from a reduction in β_2 to 5.43 (−0.60, −10%), thereby decreasing the steepness of the anion Morse branch to the right of the minimum. In this case the anion level spacing is reduced, resulting in a much narrower $\Delta v=0$ sequence band.

Increasing x_1 to 1.11 (+0.10, +10%) shifts the left boundary of the switching region between the second Morse function and the long range multipole interaction to larger *R*, i.e., essentially extends the Morse region of the anion potential on the right of the minimum. This results in a steepening of the potential, and therefore an increase of the anion level spacing and the $\Delta v=0$ sequence band spacing. Finally, we investigate the effect of increasing x_2 (which determines the right boundary of the switching region) to 1.58 (+0.15, +10%). This is expected to have an effect only on the medium range part of the anion potential. Nevertheless, deviations from the experimentally observed level spacing are found already for the 2-2 peak, and are even more apparent for the $\Delta v=-2$ sequence band (4-6, 5-7, i.e., the high v'-v'' region). All of these examples show how restricted the choice for each anion parameter is, and the high sensitivity of the simulation with respect to the x_2 variation clearly demonstrates in what detail the population of higher anion vibrational levels allows a characterization of the anion potential even at values of *R* considerably larger than R_m.

Similar analyses of the parameter sensitivity have been carried out for the potentials of the *I* and *II* states. The potential diagram in Fig. 4 clearly shows that the equilibrium bond lengths of both neutral states are considerably larger than that of the anion (see also Table V). Photodetachment from the anion (mainly the $v''=0$ level) therefore predominantly samples the repulsive wall of these states. Consequently, it is found that the key features visible in the spectra, in these cases the length and spacing of the neutral progressions in the *I* and *II* state spectra (Figs. 2 and 3 as well as Tables II and III), are particularly sensitive to the steepness of the neutral repulsive wall (β_1) and to the relative position of the potential curves (R_m). However, the spectral simulation is less sensitive with respect to the parameters β_2, x_1, and x_2 which determine the shape of the potentials at increasingly larger *R*.

For sake of clarity, the foregoing discussion has focused on the variation of only a *single* parameter relative to the best fit. We have also carried out extensive multiparameter variations to be sure that we fully explore the whole parameter space in the search for the global optimum. We have found that the narrow boundaries obtained in the single parameter variations do not change very much, i.e., counteracting deviations caused by detuning of a single parameter through changing a second or even third parameter works only for a very limited range of values. The estimated uncertainties from the latter analysis have been included in Table V.

From the location of the turning points corresponding to the highest energy levels contributing to transitions in our spectra we estimate that our XeI anion, *X*, *I*, and *II* state potentials are very well defined over the intervals $R=3.6$–4.8 Å, 3.5–5.4 Å, 4.0–5.6 Å, and 3.8–5.0 Å, respectively. This corresponds to 34%, 76%, 63%, 48% of the total well depth of these potentials (Fig. 4). Because the parameters B_4 and B_6 (C_6 and C_8) characterizing the anion (neutral) long range interactions are well-established from either experimental or *ab initio* data (Sec. IV A), and should be reliable within the range of ±15% to ±30%, the behavior of our model potentials at large *R* should also be realistic. However, the XeI^- ZEKE spectra are insensitive to the high energy region of the repulsive wall which is therefore less well characterized.

Considering the small error margins from our analysis, the largest uncertainty in our potentials is probably *systematic* in nature and linked to the uncertainties of R_m and ϵ in our reference potential, the *X* state potential of R&T. For example, each increase in the *X* state vibrational level numbering[38] by one quantum will increase ϵ_X by about 24 cm^{-1}. The same increase will apply to the well depths of all the other states [Eqs. (7)–(9)], presumably accompanied by minor adjustments of the other potential parameters. In any case our well depths are certainly lower bounds to the ''real'' values.

V. DISCUSSION

In this section we discuss our results for the XeI neutral and anion potentials and compare them to previously published results. Moreover, the surprisingly low *I* state intensity (compared to the *X* state) will be considered in more detail.

A. ZEKE potentials and results from other studies

The parameters of the *X* and *I* state potentials obtained from Lee's scattering study[36] have already been included in Table V for comparison. Our *X* state potential is essentially identical with that determined by R&T, differing only in the type of potential form employed (and the very long range part, which will not be further considered here). In contrast, the *X* state potential from the scattering experiment has a shallower well (difference >10%), and R_m is about 0.25 Å larger. Nonetheless, this can still be termed complete agreement considering the uncertainties in R_m of Lee's study and our study (both roughly ±10%). The Morse parameter β_2 of 6.29 is close to Lee's value of 6.50. However, β_1 (5.93 at the minimum and 4.70 at 3.50 Å, according to our fit) is larger than in Lee's potential (4.40), so our potential rises more rapidly for $R<R_m$.

Comparing our *I* state potential to that deduced from the scattering experiment, we see that our well depth is larger by about 4.3 meV. This is expected, however, because our potential is referenced to the deeper R&T *X* state potential. A more meaningful comparison would therefore involve the well depth difference between the *X* and *I* states; the difference between Lee's well depths is only about 1 meV larger than ours. When comparing the differences in the equilibrium distance R_m of the same states, the ZEKE results yield 0.29 Å, in nearly perfect agreement with the scattering measurements (0.30 Å). The β_1 Morse parameter of our *I* state

TABLE VI. Characteristic quantities of the ZEKE XeI^- anion potential compared to literature potentials. Uncertainties (±) given in parentheses as reported in each work cited, if available.

Source	ϵ [meV]	R_m [Å]
present work[a]	103.2	4.09
scaled electron gas[b]	144	3.85
CCSD(T)[c]	100 (43)	4.34
polarizability correlations[d]	133	4.27
modified polarizability correlations[e]	123	4.17
universal interaction potentials[f]	261 ($\geqslant$78)	3.41 ($\geqslant$1.0)
rare gas halide surface potentials[g]	75	4.20
unified perturbative approach[h]	98	4.18

[a]Possible *absolute* shift of +3 meV per unit in ϵ, if X state numbering changes as explained in the text, and of about ±0.3 Å in R_m.
[b]Reference 22.
[c]Reference 21.
[d]Reference 23.
[e]As (d), but using modified constants from Ref. 16.
[f]Reference 24.
[g]Reference 25.
[h]Reference 26.

TABLE VII. Comparison of equilibrium bond lengths R_m and well depths ϵ for rare gas iodine anion and neutral clusters extracted from anion ZEKE spectroscopy.

		ArI[a]	KrI[a]	XeI
R_m [Å]	$X1/2$	3.95	4.05	4.05
	anion	4.07	4.11	4.09
	$II1/2$	4.11	4.20	4.24
	$I3/2$	4.18	4.32	4.34
ϵ [meV]	$I3/2$	13.7	16.7	25.1
	$II1/2$	15.9	20.2	27.5
	$X1/2$	18.8	23.9	33.1
	anion	45.7	67.2	103.2

[a]Reference 17.

potential agrees very well with the scattering result. Our value for β_2, however, is considerably smaller, indicating a less steeply rising potential for $R>R_m$. Although our β_2 value is less precise than for β_1, because we are more sensitive to the region of the potential for which $R<R_m$, Lee's value for β_2 lies well outside our error bars; simulations using the higher value result in a significantly poorer fit to experiment.

The existing data for the *II* state from other sources is extremely limited. The only information available comes from XeI bound-free emission spectra by Tamagake *et al.*,[34] which gave estimates of the *II* state well depth and location ($\epsilon=10.4$ meV and $R_m=4.80$ Å, respectively). The potentials in their study are based on theoretical calculations by Hay and Dunning,[35] including an *ad hoc* dispersion correction to improve the agreement between their experiments and spectral simulations. Considering their additional results for the *X* state (17.4 meV, 4.34 Å) and *I* state (6.8 meV, 5.12 Å) it appears that their potentials systematically underestimate the well depth and overestimate the equilibrium distance for these states. Although our $II1/2\leftarrow$anion ZEKE spectrum suffers from reduced resolution, our experiment yields the first reliable potential for the *II* state, particularly for $R<R_m$.

We obtain more new information about the XeI^- anion potential. R_m is slightly shortened upon photodetachment to the *X* state (−0.04 Å), even though the anion binding energy is considerably larger (Table V). Obviously, the larger radius of the iodide anion compensates for the stronger attraction of the charge-induced multipole terms not present in the neutral.

For comparison with previous studies of this system, we have summarized available R_m and ϵ data for the XeI^- anion in Table VI. There are no other experimental results to be found for the XeI^- anion, not even ion mobility data, which is available for most of the other rare gas halide pairs.[60] The scaled electron gas theory of Waldman and Gordon yields a much higher well depth but a much shorter equilibrium bond length than we obtain.[22]

In a very recent theoretical study by Schröder *et al.*,[21] potential well depths and equilibrium bond lengths were determined at the coupled cluster level of theory for the whole series of xenon halide anions (and the respective neutral *X* states). The XeI^- well depth is very close to ours, however, the cited uncertainty is substantial. For the equilibrium bond length the calculations yielded a value which exceeds ours by 0.25 Å, and unfortunately no error limits were given.

The results of Cappelletti *et al.* in Table VI were obtained by particularly simple formulas based on empirically determined polarizability correlations.[23] Their values for R_m and ϵ both significantly exceed our values. In a very recent publication we used our ZEKE data on the ArI^-, KrI^-, $ArBr^-$,[17] $KrBr^-$, $XeBr^-$, and $KrCl^-$ anion potentials[16] to recalibrate the numerical coefficients in their formulas. When using these values the resulting well depth and equilibrium bond lengths come closer to our experimental values, but still show deviations in the same direction as observed with the original constants.

Several semi-empirical methods have been proposed in the literature. The best agreement in the case of XeI^- is found for Patil's ''unified perturbative approach,''[26] whereas the ''surface potential'' of Wilson *et al.*[25] yields a significantly lower well depth. Both ϵ and R_m predicted from the ''universal interaction potentials'' of Koutselos, Mason, and Viehland[24] deviate considerably from our values, particularly the well depth. Note also that for $KrBr^-$, $XeBr^-$, and $KrCl^-$ the difference between our most recent ZEKE results and their values is less extreme, but nevertheless substantial.[16]

In Table VII we compare the well depths and equilibrium bond lengths for the rare gas–iodine anions and corresponding neutral states studied in our group by anion ZEKE spectroscopy. For each individual rare gas iodine pair we observe the trend $R_m(X)<R_m(\text{anion})<R_m(II)<R_m(I)$, and $\epsilon(I)<\epsilon(II)<\epsilon(X)<\epsilon(\text{anion})$. The *X* state acquires predominantly Σ character at short range, which corresponds to the situation where the iodine atom approaches the rare gas with the unpaired electron on the internuclear axis. In contrast, the *I* state is a pure Π state (at all distances) and the *II* state has predominantly Π character; i.e., in these cases the unpaired electron is located perpendicular to the internuclear axis. The greater stabilization of the Σ state relative to the Π

state in rare gas halogen systems has been attributed by Aquilanti and co-workers[61] to charge transfer, resulting from configuration interaction between the lower lying neutral and higher lying ionic (Rg^+X^-) molecular states of the same symmetry. On the other hand, a recent *ab initio* study by Burcl *et al.*[62] on the HeCl, NeCl, and ArCl potentials indicates that minimization of exchange repulsion is the primary reason for a more strongly bound Σ state. It is likely that both effects are important in XeI, due to the highly polarizable Xe atom.

Coming back to Table VII we find that in all cases the anions have by far the largest well depths, which is not surprising because of the much stronger attraction due to the leading charge-induced dipole term and the additional charge-induced quadrupole contribution [Eq. (5)], in contrast to the neutrals. The anion equilibrium bond length, however, is in each case slightly larger than that of the neutral X state, for the same reasons given above. We note that the *decrease* in R_m associated with the $X1/2 \leftarrow$ anion transition becomes smaller for the heavier rare gas atoms, whereas the *increase* in R_m for the $I3/2 \leftarrow$ anion transition becomes larger.

Comparing the same states for different rare gas iodine clusters, we see that in each case $\epsilon(\mathrm{ArI}) < \epsilon(\mathrm{KrI}) < \epsilon(\mathrm{XeI})$, which is due to the increasing rare gas polarizability from Ar to Xe. However, the bond lengths for KrI and XeI are very similar for all cases. This counterintuitive result is somewhat misleading because it relies on absolute R_m values, for which the uncertainties are large. In general, the lack of precise ($<1\%$), absolute R_m values represents the most significant defect in the rare gas halogen and halide potentials; the determination of these will require spectroscopy with rotational resolution.

B. Intensity of the *I*3/2 state in the ZEKE spectra

An interesting feature of our XeI^- ZEKE spectra which has been only briefly mentioned so far is the surprisingly low intensity observed for the I state relative to the X state. To clarify this point, we show in Fig. 6 a comparison of the combined X and I state ZEKE spectra for the complete series of rare gas iodide anions (ArI^-, KrI^-, and XeI^-) studied by us so far.[17] While in the case of ArI the 0-0 transition of the I state is nearly as large as that of the X state, it is already significantly smaller in the case of KrI and almost disappears in XeI.

Although the $I3/2 \leftarrow$ anion band becomes more extended as the rare gas mass increases, Franck-Condon factors alone are insufficient to explain the trend in intensities. The vibrational stick spectrum representing the transitions to the I state had to be rescaled by factors of 0.64, 0.46,[17] and 0.10, respectively, relative to the X state before convolution with the ZEKE and rotational line shape (Sec. IV B) in order to match the experimentally observed intensity pattern. There are at least two possible explanations. The observed effect may reflect either variations in the transition moments to the two neutral states or differences in the s-wave partial detachment cross sections; due to the Wigner threshold law,[63] only those photoelectrons ejected with orbital angular momentum $l=0$ contribute to the ZEKE signal.[12]

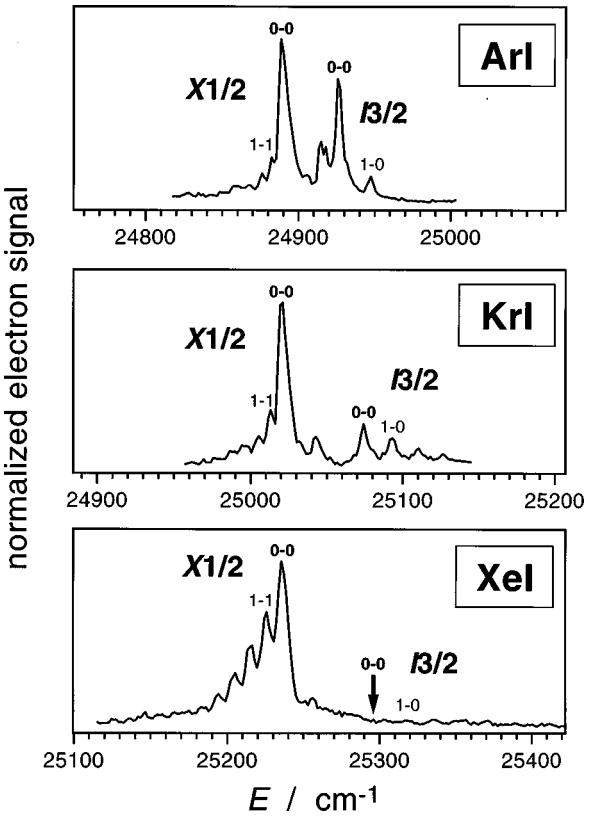

FIG. 6. Comparison of ArI^-, KrI^-, and XeI^- ZEKE spectra for the $X1/2$ and $I3/2$ states. Note the considerable drop in intensity for the $I3/2$ state features relative to the $X1/2$ state part in each spectrum with increasing rare gas size. ArI^- and KrI^- ZEKE results from Ref. 17.

To study this effect further, we have measured polarization-dependent photoelectron spectra (PES) of XeI^- at a photodetachment wavelength of 355 nm, because electronic band intensities in a photoelectron spectrum depend primarily on transition moments. The results are shown in Fig. 7, along with the ZEKE spectrum. The energy scale for the PES represents the electron binding energy. PES data at angles of $\theta=0°$ (open circles) and 90° (filled squares) between the plane of laser polarization and the direction of electron detection were recorded. Although the resolution of the photoelectron spectrum is clearly poorer than that of the ZEKE spectrum, we observe a large broad main peak where the X state transitions in the ZEKE spectrum are located, and a smaller but pronounced shoulder at higher energy, where the I state transitions in the ZEKE spectrum are found. The relative intensities of the PES features show only a small dependence upon laser polarization angle.

To compare the ZEKE results to the PES data, the ZEKE results have to be converted in an appropriate fashion. Because of the good quality of the spectral fit in Fig. 2 we have directly taken the vibrational stick spectrum forming the basis of this simulation (including the aforementioned scale factor of 0.10) and convoluted it with a Gaussian of 8 meV FWHM, which should accurately represent the resolution of the anion photoelectron spectrometer at this electron kinetic energy of roughly 0.4 eV. The resulting ''ZEKE-based PES'' is shown as a dotted line in Fig. 7, denoted as ''Conv. I''. The X band is fit quite well, but the I band in this con-

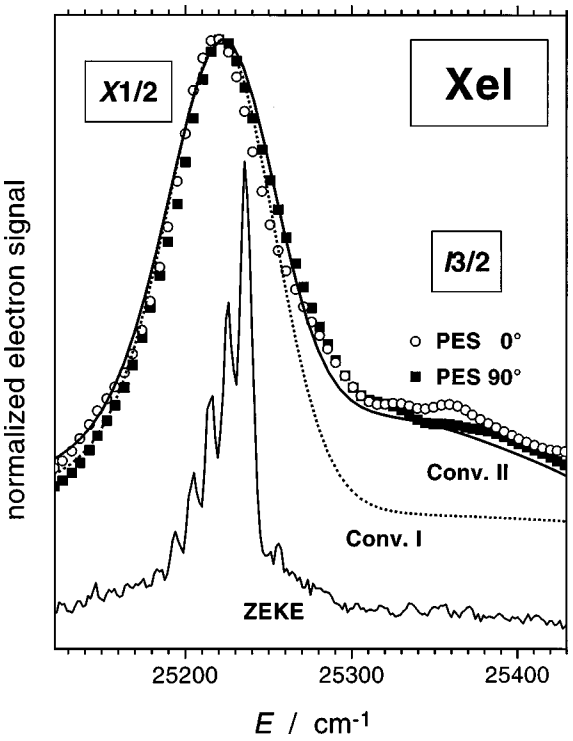

FIG. 7. Comparison of polarization-dependent XeI^- photoelectron spectra for the $X1/2$ and the $I3/2$ states with convolutions based on the corresponding ZEKE spectrum. Open circles: PES spectra for $\theta=0°$ (angle between laser polarization plane and direction of electron extraction), filled squares: same, but for $\theta=90°$; lower solid line: ZEKE spectrum from Fig. 2; dotted line ''Conv. I'': result of a convolution of the vibrational stick spectrum underlying the ZEKE best fit simulation from Fig. 2 with an 8 meV Gaussian line shape characteristic for the PES resolution at this electron kinetic energy; solid line ''Conv. II'': same, but the vibrational sticks belonging to the $I3/2$ part of the spectrum have *not* been scaled down in intensity before convolution with the PES line shape. The PES spectra and convolutions are normalized to the same maximum, and the ZEKE spectrum has been shifted down for the sake of clarity. Note the eye-catching difference of the two convolutions for $E>25\,250\ cm^{-1}$.

volution is clearly too weak. However, if the stick spectrum is not rescaled prior to convolution, we obtain ''Conv. II'', which nicely matches the experimental photoelectron spectrum; i.e., the *I* state intensities now almost coincide.

This comparison indicates that the transition moments for photodetachment to the *X* and *I* states are indeed similar, and suggests that the low intensity of the *I* state in the ZEKE spectrum comes from a small *s*-wave partial detachment cross section near the detachment threshold. While the polarization dependence of the photoelectron spectrum also depends on the partial wave decomposition of the ejected photoelectrons, it is taken at a photon energy well above the detachment threshold where the partial wave decomposition can be very different.

The results in Fig. 6 and in our previous studies of rare gas bromides and chlorides[16,64] show that this intensity effect in the ZEKE spectrum becomes more pronounced as the rare gas atom becomes larger and the halide smaller. This trend correlates with increasing binding energy in the anion, and with increasing anisotropy in the neutral. The latter effect can be tracked by the difference in the well depths between the *X* and *I* states, which have predominant Σ and pure Π character, respectively. It also appears that the intensity of the *II* state, which has mainly Π character, correlates with that of the *I* state, although this is more difficult to quantify because detachment to the *II* state generally requires frequency doubling of the dye laser output with an accompanying loss of laser pulse energy. Thus interactions in the anion and neutral which result in more differentiation of the σ and π orbitals from which detachment occurs (i.e., that correlate to the *p*-orbitals on the isolated halide) lead to differences in the *s*-wave partial detachment cross sections near threshold for the two types of orbitals.

VI. CONCLUSIONS

In our study of the XeI^- anion by ZEKE and photoelectron spectroscopy we have characterized the anion and neutral potentials involved in the photodetachment of this prototypical diatomic rare gas halide cluster in considerable detail. A simulation of the ZEKE spectra for the $X1/2$, $I3/2$, and $II1/2$ states accessible by the photodetachment process has allowed an assignment of essentially all features in the spectra, even those having very low intensity.

We have extracted model potentials for all states involved which define the *relative* positions and shapes of all electronic states in the Franck-Condon region with high accuracy. We have underlined this by an extensive test of the sensitivity of the potential parameters for each state. However, to be able to pinpoint the *absolute* position of all potentials, we need external experimental information on one of the four potential curves as a reference. In this case, we used the *X* state potential previously determined by Radzykewycz and Tellinghuisen, obtained from $X\leftarrow B$ emission studies.[38]

The ZEKE data are fully consistent with the *X* state potential from the emission study, whereas some differences between the ZEKE *I* state potential and the earlier *I* state potential from scattering data are observed. We obtain the first accurate potentials of the *II* state and the XeI^- anion, although worse experimental resolution in the case of the *II* state ZEKE spectrum makes this potential somewhat less reliable than the others. Characteristic quantities like the equilibrium bond length R_m and well depth ϵ for all XeI anion and neutral potentials are consistent with trends observed in our previous ZEKE studies of the other rare gas iodides KrI^- and ArI^-.[17]

Another interesting feature is the very low intensity of the *I* state relative to the *X* state in the ZEKE spectra for XeI^- and some of the other rare gas halides. The intensity is found to decrease with increasing size of the rare gas and decreasing size of the halide. The photoelectron spectrum taken for XeI^-, however, shows a much higher intensity in the *I* state region than the ZEKE spectrum, indicating that the low ZEKE intensity is probably due to pronounced differences in the *s*-wave partial detachment cross sections to both states. This trend appears to correlate with increasing binding energy in the anion and anisotropy in the neutral.

Very recently we obtained results for larger Xe_nI^- clusters up to $n=14$. A preliminary analysis of the experimental data suggests that a slight systematic increase in R_m for all XeI potentials might describe the observed trends in the clus-

ter size dependent electron affinities better. This will be considered in more detail in a forthcoming publication.[65] Together with additional results obtained for other rare gas halide clusters, e.g., Ar_nCl^-,[64] this will certainly yield further insight into the rare gas halogen and halide pair potentials and also the many-body interactions that govern bonding and structure in larger Rg_nX^- species.

ACKNOWLEDGMENTS

This research is supported by the Air Force Office of Scientific Research under Grant No. F49620-97-1-0018. T. Lenzer is grateful to the Deutsche Forschungsgemeinschaft for a postdoctoral fellowship, and M. R. Furlanetto thanks the National Science Foundation for a predoctoral fellowship. K. R. Asmis gratefully acknowledges financial support by the Swiss National Science Foundation.

[1] G. C. Maitland, M. Rigby, E. B. Smith, and W. A. Wakeham, *Intermolecular Forces* (Oxford University Press, Oxford, 1981).
[2] R. A. Aziz, in *Inert Gases*, edited by M. L. Klein (Springer Verlag, Berlin, 1984), pp. 5–86.
[3] G. Chalasinski and M. M. Szczesniak, Chem. Rev. **94**, 1723 (1994).
[4] J.-H. Choi, K. T. Kuwata, Y.-B. Cao, and M. Okumura, J. Phys. Chem. A **102**, 503 (1998).
[5] M. S. Johnson, K. T. Kuwata, C.-K. Wong, and M. Okumura, Chem. Phys. Lett. **260**, 551 (1996).
[6] P. Ayotte, C. G. Bailey, G. H. Weddle, and M. A. Johnson, J. Phys. Chem. A **102**, 3067 (1998).
[7] C. G. Bailey, J. Kim, C. E. H. Dessent, and M. A. Johnson, Chem. Phys. Lett. **269**, 122 (1997).
[8] J. M. Lisy, Int. Rev. Phys. Chem. **16**, 267 (1997).
[9] C. J. Weinheimer and J. M. Lisy, Int. J. Mass Spectrom. Ion Processes **159**, 197 (1996).
[10] H. Linnartz, T. Speck, and J. P. Maier, Chem. Phys. Lett. **288**, 504 (1998).
[11] T. Speck, H. Linnartz, and J. P. Maier, J. Chem. Phys. **107**, 8706 (1997).
[12] T. N. Kitsopoulos, I. M. Waller, J. G. Loeser, and D. M. Neumark, Chem. Phys. Lett. **159**, 300 (1989).
[13] K. Müller-Dethlefs, M. Sander, and E. W. Schlag, Z. Naturforsch. Teil A **39**, 1089 (1984).
[14] K. Müller-Dethlefs, M. Sander, and E. W. Schlag, Chem. Phys. Lett. **112**, 291 (1984).
[15] K. Müller-Dethlefs and E. W. Schlag, Annu. Rev. Phys. Chem. **42**, 109 (1991).
[16] I. Yourshaw, T. Lenzer, G. Reiser, and D. M. Neumark, J. Chem. Phys. **109**, 5247 (1998).
[17] Y. Zhao, I. Yourshaw, G. Reiser, C. C. Arnold, and D. M. Neumark, J. Chem. Phys. **101**, 6538 (1994).
[18] I. Yourshaw, Y. Zhao, and D. M. Neumark, J. Chem. Phys. **105**, 351 (1996).
[19] Y. Zeiri, J. Phys. Chem. A **102**, 2785 (1998).
[20] I. Becker, G. Markovich, and O. Cheshnovsky, Phys. Rev. Lett. **79**, 3391 (1997).
[21] D. Schröder, J. N. Harvey, M. Aschi, and H. Schwarz, J. Chem. Phys. **108**, 8446 (1998).
[22] M. Waldman and R. G. Gordon, J. Chem. Phys. **71**, 1325 (1979).
[23] D. Cappelletti, G. Liuti, and F. Pirani, Chem. Phys. Lett. **183**, 297 (1991).
[24] A. D. Koutselos, E. A. Mason, and L. A. Viehland, J. Chem. Phys. **93**, 7125 (1990).
[25] J. W. Wilson, J. H. Heinbockel, and R. A. Outlaw, J. Chem. Phys. **89**, 929 (1988).
[26] S. H. Patil, J. Chem. Phys. **89**, 6357 (1988).
[27] V. Aquilanti, D. Cappelletti, V. Lorent, E. Luzzatti, and F. Pirani, J. Phys. Chem. **97**, 2063 (1993).
[28] H. Haberland, Z. Phys. A **307**, 35 (1982).
[29] A. J. Conley, J.-Y. Fang, and C. C. Martens, Chem. Phys. Lett. **272**, 103 (1997).
[30] J.-Y. Fang and C. C. Martens, J. Chem. Phys. **105**, 9072 (1996).
[31] J. J. Ewing and C. A. Brau, Phys. Rev. A **12**, 129 (1975).
[32] J. Tellinghuisen, A. K. Hays, J. M. Hoffman, and G. C. Tisone, J. Chem. Phys. **65**, 4473 (1976).
[33] M. P. Casassa, M. F. Golde, and A. Kvaran, Chem. Phys. Lett. **59**, 51 (1978).
[34] K. Tamagake, D. W. Setser, and J. H. Kolts, J. Chem. Phys. **74**, 4286 (1981).
[35] P. J. Hay and T. H. Dunning, Jr., J. Chem. Phys. **69**, 2209 (1978).
[36] P. Casavecchia, G. He, R. K. Sparks, and Y. T. Lee, J. Chem. Phys. **77**, 1878 (1982).
[37] R. B. Jones, J. H. Schloss, and J. G. Eden, J. Chem. Phys. **98**, 4317 (1993).
[38] D. T. Radzykewycz and J. Tellinghuisen, J. Chem. Phys. **105**, 1330 (1996).
[39] C. C. Arnold, Y. Zhao, T. N. Kitsopoulos, and D. M. Neumark, J. Chem. Phys. **97**, 6121 (1992).
[40] T. N. Kitsopoulos, Ph.D. thesis, University of California, Berkeley (1991).
[41] C. C. Arnold, Ph.D. thesis, University of California, Berkeley (1994).
[42] R. B. Metz, A. Weaver, S. E. Bradforth, T. N. Kitsopoulos, and D. M. Neumark, J. Phys. Chem. **94**, 1377 (1990).
[43] D. W. Arnold, S. E. Bradforth, E. H. Kim, and D. M. Neumark, J. Chem. Phys. **102**, 3493 (1995).
[44] T.-K. Ha, Y. He, J. Pochert, M. Quack, R. Ranz, G. Seyfang, and I. Thanopoulos, Ber. Bunsenges. Phys. Chem. **99**, 384 (1995).
[45] D. Hanstorp and M. Gustafsson, J. Phys. B **25**, 1773 (1992).
[46] A. D. Koutselos and E. A. Mason, J. Chem. Phys. **85**, 2154 (1986).
[47] E. A. Mason and E. W. McDaniel, *Transport Properties of Ions in Gases* (Wiley, New York, 1988).
[48] A. Kumar and W. J. Meath, Mol. Phys. **54**, 823 (1985).
[49] C. Hättig and B. A. Heß, J. Phys. Chem. **100**, 6243 (1996).
[50] K. Andersson and A. J. Sadlej, Phys. Rev. A **46**, 2356 (1992).
[51] L. J. Bartolotti, L. Ortiz, and Q. Xie, Int. J. Quantum Chem. **49**, 449 (1994).
[52] M. V. K. Sastri, P. L. Narasimhulu, and K. D. Sen, J. Chem. Phys. **80**, 584 (1984).
[53] C. Hättig and B. A. Heß, J. Chem. Phys. **108**, 3863 (1998).
[54] ORIGIN 5.0, Microcal Software Inc., Northampton, MA 01060 (1997).
[55] J. C. Light, I. P. Hamilton, and J. V. Lill, J. Chem. Phys. **82**, 1400 (1985).
[56] E. M. Greenawalt and A. S. Dickinson, J. Mol. Spectrosc. **30**, 427 (1969).
[57] V. Aquilanti, G. Liuti, F. Pirani, and F. Vecchiocattivi, J. Chem. Soc., Faraday Trans. 2 **85**, 955 (1989).
[58] V. Aquilanti and G. Grossi, J. Chem. Phys. **73**, 1165 (1980).
[59] W. G. Lawrence and V. A. Apkarian, J. Chem. Phys. **101**, 1820 (1994).
[60] L. A. Viehland and C. C. Kirkpatrick, Chem. Phys. **202**, 285 (1996).
[61] V. Aquilanti, D. Cappelletti, and F. Pirani, Chem. Phys. Lett. **271**, 216 (1997).
[62] R. Burcl, R. V. Krems, A. A. Buchachenko, M. M. Szczesniak, G. Chalasinski, and S. M. Cybulski, J. Chem. Phys. **109**, 2144 (1998).
[63] E. P. Wigner, Phys. Rev. **73**, 1003 (1948).
[64] T. Lenzer, I. Yourshaw, G. Reiser, M. R. Furlanetto, and D. M. Neumark, J. Chem. Phys. (to be published).
[65] T. Lenzer, M. R. Furlanetto, N. Pivonka, and D. M. Neumark, J. Chem. Phys. (to be published).